Title: Experimental assessment of thermodynamic stability and nucleation of NiO in liquid lead-bismuth eutectic for MYRRHA

Authors: **Aleksandr Tsybanev**[a,b,*], Alessandro Marino[a], Lim Jun[a], Kristof Gladinez[c] and Nele Moelans[b]

[a] SCK CEN (Belgium Nuclear Research Center), Boeretang 200, Mol 2400, Belgium
[b] KU Leuven, Kasteelpark Arenberg 44, Leuven 3001, Belgium
[c] Olpas, Slachthuisstraat 96, Turnhout 2300, Belgium
* corresponding author, Aleksandr.tsybanev@sckcen.be

Abstract

MYRRHA is an accelerator-driven system with a primary coolant of liquid lead-bismuth eutectic (LBE). Nickel, a major corrosion products released in LBE during normal operation, can potentially form oxides and intermetallic compounds with bismuth. This study focuses on the behavior of dissolved nickel and the conditions for nickel oxide (NiO) formation in LBE.

We first measured the dissolved oxygen concentration (DOC) at the NiO equilibrium from 225 to 500 °C across three levels of nickel concentration. These measurements showed a deviation from the trend expected from literature, particularly in the range of 325-400 °C. Based on the measurements, we proposed the activity coefficient of Ni in LBE within this temperature range. Secondly, we identified the conditions for NiO nucleation by cyclically varying the temperature of LBE at high nickel concentration and different DOC levels. Based on these observations, we concluded that NiO nucleation is unlikely under the MYRRHA operating conditions (200-400 °C, 10^{-7}-10^{-6} wt.%).

Keywords: lead-bismuth eutectic, NiO, Ni-Bi intermetallic, nickel activity, nucleation

1 Introduction

MYRRHA (Multi-purpose hYbrid Research Reactor for High-tech Applications) is an accelerator-driven system under development at SCK CEN, Belgium [1]. Liquid lead-bismuth eutectic (LBE), chosen as the coolant for the MYRRHA reactor, is known to be corrosive to stainless steels [2]. To mitigate corrosion, a passivation oxide scale can be promoted on the steel surface by controlling the dissolved oxygen concentration (DOC) at the steel/liquid interface to a level sufficient for the formation of the protective layer [3]. However, studies show that at long exposures this protective oxide layer formed *in-situ* tends to fail locally [4]. This leads to a local degradation of the solid material through dissolution of the solid steel components. As there is no data on the tendency of the oxide layer to repassivate, a limited but continuous release of steel constituents, such as iron, chromium and nickel, is expected in the LBE over time. Their possible chemical interactions with dissolved oxygen could affect the reactor's operation; therefore, understanding these interactions is essential.

From the coolant chemistry control, chemical interactions of corrosion products and their derivatives (e.g. Co, a product of iron neutron activation) have to be characterized in order to avoid unexpected formation and dissolution of solid compounds that could disturb the normal operation of the reactor (e.g. deposition on cold surfaces). As stainless steel is the cladding of the MYRRHA fuel rods, Ni is one of the main corrosion products expected in LBE, besides Fe and Cr, due to its high concentration in the steel and its high solubility in LBE [5]. While several research papers have investigated the formation of magnetite (Fe_3O_4) [6],

hematite (Fe_2O_3) [7], cobalt oxide (CoO) [8] and Bi_3Ni intermetallic [9] in the bulk of LBE, the formation of nickel oxides has not yet been properly addressed.

Potentially, the following two chemical reactions are possible between dissolved nickel and oxygen in LBE. The first reaction is the formation of NiO Eq.(1.1), which is a reliably defined single basic oxide of nickel [10]. The second reaction is a reaction on suspended Fe_3O_4 particles leading to the formation of Fe_2NiO_4 Eq.(1.2). The latter reaction is chosen because of the presence of Fe_3O_4 in LBE: (i) it has been confirmed to dissolve and precipitate upon temperature changes [6,11] and (ii) it can react with dissolved oxygen, e.g. the Fe_3O_4-Fe_2O_3 reaction [7]. The Fe_3O_4-Fe_2O_3 reaction is observed in the LBE used in the present study, thus confirming the presence of Fe_3O_4 particles in our experiments.

$$Ni(lbe) + O(lbe) = NiO(s) \quad (1.1)$$

$$3Ni(lbe) + 2Fe_3O_4(s) + 4O(lbe) = 3Fe_2NiO_4(s) \quad (1.2)$$

Concerning the Ni chemistry in LBE, studies in the literature have focused on the formation of Bi-Ni intermetallic compounds, namely Bi_3Ni and BiNi [12], because Bi_3Ni in particular caused a plugging problem in the LBE-containing CORRIDA loop at KIT [13]. *Martinelli et al.* [5] identified two regions of the solubility of nickel in LBE which are separated by Bi_3Ni formation below 415 °C. *Gregori et al.* [9] measured the Bi_3Ni equilibrium with a nickel oxide in LBE below 322 °C. Performed consistently and on a solid basis, these studies, however, do not agree well with each other. As compared in [9], these studies produce two different trends of nickel activity in LBE. This leads to a misestimation of the true nickel activity in LBE, and hence the dissolved nickel concentration for the formation of Bi_3Ni.

More detailed thermodynamic calculations showed that equilibrium Eq. (1.1) and Eq. (1.2) require less dissolved nickel than the intermetallics in the presence of dissolved oxygen [7]. In other words, the nickel oxides – mainly NiO – could potentially eliminate the formation of Bi_3Ni by consuming dissolved nickel due to the continuous supply of oxygen for steel passivation. To evaluate this possibility and to better understand the chemistry of Ni in LBE, the present study focused on the thermodynamic stability and nucleation of NiO in isothermal small-scale LBE setups. First, after controlled addition of Ni to LBE, we measured the dissolved oxygen concentration (DOC) at equilibrium in 225-500 °C. From these measurements, we derived the activity coefficients of nickel in LBE in 300-500 °C, which brought the solubility data [5] and the $Ni_{(lbe)}$-Bi_3Ni measurements [9] into agreement. Secondly, we determined the conditions for NiO nucleation in LBE with 436 ± 36 ppmw Ni by conducting thermal cycling experiments (cyclically varying the temperature of LBE [7]). Based on these measurements, bulk NiO nucleation and NiO nucleation on PbO were found improbable under the MYRRHA operating conditions – 10^{-6}-10^{-7} wt.% DOC, 200-400 °C and approximately 10 ppmw Ni.

2 Theory

2.1. Excess Gibbs energy for dilute Ni in LBE

In a binary solution A-B, the interaction of A and B in the solution is modelled by the function of the excess Gibbs energy ${}^{E}G_m$ [14]. It is usually defined in such a way that it goes to zero for the end-members, pure solutions of A and B. Now consider a ternary solution of Ni and LBE. If the amount of Ni is negligibly small, then its addition and the possible chemical reactions with Bi will not change the composition of LBE. In this case it would be convenient to define the total excess Gibbs energy in such a way that it goes to zero for

pure LBE and pure Ni solutions. In other words, we select as the end-members, also referred to as 'reference states', pure liquid nickel and pure liquid LBE.

Since the Gibbs free energy has the property of additivity, the ${}^{E}G_m$ of the LBE-Ni solution can be expressed as the sum of the nickel contribution and the LBE contribution Eq.(3).

$$ {}^{E}G_m = x_{Ni} \cdot {}^{E}G_{Ni} + (1 - x_{Ni}) \cdot {}^{E}G_{LBE} \qquad (3) $$

with ${}^{E}G_{Ni}$ and ${}^{E}G_{LBE}$ the partial excess Gibbs energy of Ni and LBE in the LBE-Ni solution, respectively, x_{Ni} and $(1 - x_{Ni})$ the molar fraction of Ni and LBE in the LBE-Ni solution, respectively.

For small amounts of Ni, we can apply Henry's law for Ni, for which the ${}^{E}G_{Ni}$ is independent of the solution composition, but can be a function of temperature Eq.(4). Henry's law for Ni consequently leads to Raoult's law for LBE, i.e. Ni does not affect LBE, so the ${}^{E}G_{LBE}$ is close to zero. Therefore, the total excess Gibbs energy is completely determined by the contribution of Ni in Eq.(3). The same conclusion applies to the ${}^{E}G_m$ of the Pb-Ni and Bi-Ni binaries at high Ni dilution.

$$ {}^{E}G_{Ni} = RT \ln {}^{l}\gamma_{Ni} \qquad (4) $$

with ${}^{l}\gamma_{Ni}$ the activity coefficient of Ni in the LBE-Ni solution w.r.t. pure liquid Ni.

The activity coefficient in Eq.(4) can be derived from direct electrochemical measurements, as has been done for dissolved oxygen in LBE [15], or from solubility measurements. As we cannot directly measure the activity of nickel in LBE, we rely on the solubility data from the literature. The activity coefficient is the reciprocal of the solubility S_{Ni} Eq.(5) when dissolved nickel is in equilibrium with solid nickel (denoted as Ni(s) referring to Ni(FCC)). The derivation of Eq. (5) is given in Appendix A1.

$$ \ln {}^{s}\gamma_{Ni} = - \ln S_{Ni} \qquad (5) $$

In Eq.(5) γ_{Ni} is determined w.r.t. pure Ni(s), whereas in Eq.(4) γ_{Ni} is required w.r.t pure liquid nickel. The change in reference state is explained in detail in Appendix A2. The final expression is given in Eq.(6).

$$ \ln {}^{l}\gamma_{Ni} = \ln {}^{s}\gamma_{Ni} + (^{\circ}\mu_{Ni(s)} - {}^{\circ}\mu_{Ni(l)}) / RT = - \ln S_{Ni} + (^{\circ}\mu_{Ni(s)} - {}^{\circ}\mu_{Ni(l)}) / RT \qquad (6) $$

with ${}^{s}\gamma_{Ni}$ and ${}^{l}\gamma_{Ni}$ the activity coefficient w.r.t. pure Ni(s) and Ni(l), respectively, $^{\circ}\mu_{Ni(s)}$ and $^{\circ}\mu_{Ni(l)}$ the chemical potentials of pure Ni(s) and Ni(l) [16].

Combined together, Eq.(4) and Eq.(6) provide a way to link the solubility data to the total excess Gibbs energy of the solution.

2.2. Nickel solubility in LBE

In pure bismuth, Ni can precipitate in its solid form Ni(s) or as two intermetallic compounds BiNi and Bi_3Ni with melting points of 654 °C and 471 °C, respectively [12]. By measuring and analyzing the solubility of Ni in LBE, *Martinelli et al. (2010)* [5] identified two ranges, Eq. (7.1) and Eq. (7.2) which are given in wt.%.

$$ \log_{10} C_{Ni} = 5.2 \pm 0.12 - 3500 / T, [K] \qquad \text{for 330-415 °C} \qquad (7.1) $$

$$ \log_{10} S_{Ni} = 1.7 \pm 0.08 - 1009 / T, [K] \qquad \text{for 415-900 °C} \qquad (7.2) $$

In the low-temperature region, Eq. (7.1), the authors demonstrated equilibrium with Bi_3Ni by XRD analysis of precipitates removed from the LBE at 330 °C. In the high-temperature region, Eq. (7.2), the authors

conclude that 'only one phase exists in equilibrium with the dissolved nickel in LBE' referring to the data of [17]. Since this high-temperature range includes the BiNi melting point, BiNi formation is excluded and this 'phase' is expected to be pure Ni(s). Therefore, the high-temperature nickel solubility S_{Ni} allows for a straightforward calculation of the activity coefficient via Eq. (5) or Eq. (6).

Note carefully that our choice of notation is deliberate: C_{Ni} over S_{Ni} in Eq. (7.1). We emphasize the difference between the nickel solubility when Ni(lbe) is in equilibrium with Ni(s) Eq. (7.2) and the limiting concentration of nickel due to the formation of Bi_3Ni Eq. (7.1). Because S_{Ni} is used to derive the activity coefficient ${}^s\gamma_{Ni}$, while C_{Ni} is used to calculate the activity of nickel when Bi_3Ni forms (last column in Table 1).

2.3. NiO and Fe_2NiO_4 equilibrium in LBE

The solubility product of reactions Eq. (1.1) and Eq. (1.2) can be expressed by Eq. (8.1) and Eq. (8.2) respectively. The reference states are Ni(s) and O2(g) at 1 bar and 25 °C.

NiO: $$ln\ a_{Ni} \cdot a_O = \Delta_f°G_{NiO} / RT = 10.50 - 28470.47 / T \quad (8.1)$$

Fe_2NiO_4: $$ln\ a_{Ni}^3 \cdot a_O^4 = (3 \cdot \Delta_f°G_{Fe2NiO4} - 2 \cdot \Delta_f°G_{Fe3O4}) / RT = 12.01 - 29750.34 / T \quad (8.2)$$

with a_X the activity of species X in LBE, $\Delta_f°G_X$ the standard Gibbs energy of formation of species X [9,17].

Due to low concentrations, dissolved nickel and oxygen obeys Henry's law in LBE Eq. (9).

$$a_X = \gamma_X \cdot C_X \quad (9)$$

with γ_X the activity coefficient of species X, C_X the concentration of species X. For dissolved oxygen $O_{(lbe)}$, the activity coefficient is Sievert's constant, $log_{10}\ k(1 / wt.\%) = 3.12 - 7072 / T(K)$, as defined by [15].

Combining Eq.(8.1) and Eq. (8.2) with Eq.(9), we express the solubility product in terms of the concentrations of $Ni_{(lbe)}$ and $O_{(lbe)}$, Eq. (10.1) and Eq. (10.2)[1] respectively, as in [7] (concentration is in wt.%). The NiO solubility product Eq. (10.1) agrees with the calculated expression in [19].

NiO: $$ln\ C_{Ni} \cdot C_O = 7.23 - 14509.90 / T \quad (10.1)$$

Fe_2NiO_4: $$ln\ C_{Ni}^3 \cdot C_O^4 = 31.04 - 60833.05 / T \quad (10.2)$$

Now we can compare the stability of NiO and Bi_3Ni in LBE using the solubility product of NiO Eq. (10.1) and the nickel solubility when Bi_3Ni is stable Eq. (7.1). According to Eq. (7.1), Bi_3Ni is stable at 64 ppmw of dissolved Ni in LBE at 200 °C. At this temperature, NiO is stable at 7 ppmw of Ni if the dissolved oxygen concentration (DOC) is 10^{-7} wt.% according to Eq. 10.1. If the DOC is $2 \cdot 10^{-7}$ wt.%, then NiO is stable at a lower nickel level – 3 ppmw of Ni. In the MYRRHA reactor, oxygen is to be continuously supplied to LBE to passivate the stainless steel surfaces. Therefore, NiO can potentially form and consume dissolved nickel, thus preventing Bi_3Ni formation.

Recently, *Gregori et al (2024)* [9] confirmed the formation of Bi_3Ni in LBE by measuring the equilibrium between $Ni_{(lbe)}$, Bi_3Ni and nickel oxides in 250-330 °C. Fig. 1 compares their measurements ($Ni_{(lbe)}$-Bi_3Ni) with the DOC from Eq. (10.1) and Eq. (10.2) assuming 0.02 wt.% (or 200 ppmw Ni). This dissolved nickel concentration corresponds to the lowest nickel concentration used in our experiments. Extended further,

[1] In [7], the authors calculated the Fe_2NiO_4 solubility product assuming $H(Fe_2NiO_4)$ = -1070.9 kJ/mol instead of −1074.01 kJ/mol, as they intended. In the present paper, we use the correlation calculated with -1070.9 kJ/mol.

the NiO and Fe_2NiO_4 lines would cross the $Ni_{(lbe)}$-Bi_3Ni region, marking the temperature at which 200 ppmw Ni is sufficient for Bi_3Ni formation, thus splitting Fig. 1 into two temperature regions.

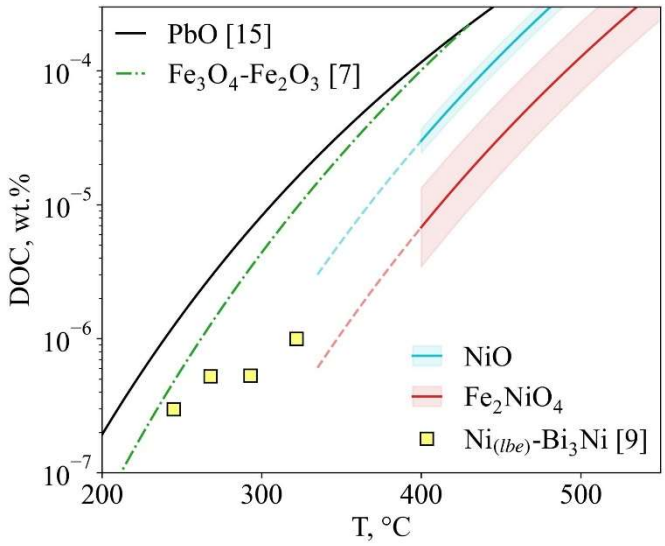

Figure 1. Equilibrium of nickel oxides with 200 ppmw of dissolved nickel in LBE:
Color-shadowed areas represent uncertainties of calculations. The PbO line corresponds to the equilibrium of PbO, also known as "oxygen saturation limit".

Below this temperature, the NiO and Fe_2NiO_4 lines must follow the $Ni_{(lbe)}$-Bi_3Ni region because Bi_3Ni formation becomes dominant in the LBE due to the excess of Bi over Ni in LBE. Its formation consumes $Ni_{(lbe)}$, which in turn dictates a higher DOC according to Eq. (10.1) and Eq. (10.2). Without thermodynamic data of Bi_3Ni, it is therefore impossible to identify which oxide is in equilibrium with Bi_3Ni in this region, NiO or Fe_2NiO_4.

Above this temperature, both oxides can be formed in undersaturated LBE (below PbO) and can be easily distinguished from each other and from the Fe_3O_4-Fe_2O_3 reaction. Furthermore, since Fe_2NiO_4 is limited by the amount of iron, its complete formation can be observed upon steady cooling, similar to the Fe_3O_4-Fe_2O_3 reaction [7]. Once Fe_2NiO_4 is fully formed, NiO begins to form on further cooling; allowing both oxides to be identified.

2.4. Stoichiometric conditions of NiO and Fe_2NiO_4

To identify which nickel oxide forms in LBE, we can characterize the stoichiometric ratio of the oxide formed, rather than relying solely on Eq. (10.1) and Eq. (10.2), which depend on the choice of γ_{Ni}. Combining Eq.(8.1) and Eq.(8.2) with Eq. (9) for two different levels of nickel, ${}^1C_{Ni}$ and ${}^2C_{Ni}$, we obtain Eq. (11.1) and Eq. (11.2). These two equations allow us to distinguish between NiO and Fe_2NiO_4 on the basis of the known ratio of C_{Ni} and the ratio of measured a_O.

NiO: $$ {}^1a_O / {}^2a_O = {}^2C_{Ni} / {}^1C_{Ni} \qquad (11.1)$$

Fe_2NiO_4: $$ ({}^1a_O / {}^2a_O)^{4/3} = {}^2C_{Ni} / {}^1C_{Ni} \qquad (11.2)$$

2.5. Driving force of nucleation

According to the classical nucleation theory, the higher the driving force for nucleation, the lower the nucleation barrier [20, 21]. Eq. (12) expresses the driving force for NiO nucleation in terms of concentrations, since Eq. (10.1) already takes into account the activity coefficient of $Ni_{(lbe)}$ and Sievert's constant of $O_{(lbe)}$.

$$I = RT \ln \left(\frac{C_{Ni} \cdot C_O}{K_{eq}(T)} \right)^{1/2} \qquad (12)$$

with K_{eq} the solubility product (or equilibrium constant) of reaction Eq. (1.1) defined by Eq. (10.1).

In Eq. (12), assume a constant C_O but a decreased C_{Ni}. To maintain the same driving force I, the equilibrium constant K_{eq} must also decrease, which in turn requires a decrease in temperature. In other words, the lower the $Ni_{(lbe)}$ concentration, the lower the temperature required to trigger NiO nucleation at the same DOC. We use this theoretical trend as a basis for measuring NiO nucleation at a high $Ni_{(lbe)}$ concentration because if it is hardly possible under these conditions, it is probably impossible at a low $Ni_{(lbe)}$ concentration.

3 Experimental

3.1 Experimental setups

Two identical experimental setups were used in the present study. Each setup consisted of a small stainless steel autoclave wrapped with heating wires and containing an alumina crucible with a molten LBE batch (ca. 1.5-2.0 kg of LBE) inside. The autoclave was sealed and kept under a slight overpressure (150-200 mbar) with a continuous flow of nitrogen (15-20 ml/min) to isolate the LBE batch from atmospheric oxygen. The DOC was measured electrochemically by an oxygen sensor [15]. Nernst's equation Eq. (13) correlates the measured potential difference ΔE at temperature T with the $O_{(lbe)}$ activity $a_{O(lbe)}$, or the DOC via the temperature-dependent Sievert constant k_S [15].

$$\Delta E = \frac{RT}{4F} \cdot \ln \frac{a_{O_2,ref}}{a_{O(lbe)}{}^2} = \frac{RT}{2F} \cdot \ln \frac{\sqrt{a_{O_2,ref}}}{C_O \cdot k_S} \qquad (13)$$

with $a_{O2,ref}$ the activity of oxygen on the reference electrode. For an air-reference oxygen sensor, the $a_{O2,ref}$ is equal to the partial pressure of oxygen in the air (0.20946 bar) [15].

Two methods were used to control the DOC: electrochemical oxygen pumping and cover gas (N_2 + 4% H_2 gas flow), as described elsewhere [7,8,11]. A K-type thermocouple was inserted into an oxygen sensor to measure the LBE temperature. In one setup (setup 2), there was a possibility to insert an impeller to stir LBE. More details about the setup design are given in [7].

3.2. Materials

LBE was supplied by 5N Plus Belgium. Several pieces of LBE were cut from the ingots and melted in an alumina crucible of each setup. After complete melting, the LBE was gently stirred and solid impurities were skimmed off the surface, similar to the procedure described in [7]. The composition of the LBE impurities was determined by neutron activation analysis (Appendix A3). The final mass of the LBE batches used in the study was 1814 ± 2 g (setup 1) and 1451 ± 2 g (setup 2).

Nickel wire Puratronic™ was purchased from Thermo Fisher Scientific® – 99.999 % purity, 0.04 inches (*ca.* 0.1 cm) diameter.

3.3. Nickel dissolution

To introduce Ni pieces, both setups had an additional port with a stainless steel rod that could slide in and out of the LBE without losing overpressure in the setup. An alumina cylinder was screwed to the tip of the rod, around which a segment of Ni wire of known mass (accuracy ± 0.1 mg) could be wrapped to avoid possible flotation of Ni due to the high density of LBE. For each Ni addition, the stainless steel rod was kept in the LBE at 500 °C for at least 20 hours, after which the stainless steel rod was removed from the LBE. Prior to Ni addition, the DOC was reduced to ca. 10^{-9} wt. % at 500 °C.

In setup 1, a single piece of Ni wire corresponding to 203.2 ppmw Ni was dissolved (LBE+200Ni). In setup 2, two pieces of Ni wire (500.5 and 507.6 ppmw Ni respectively) were dissolved in sequence to study LBE with 500.5 ppmw Ni (LBE+500Ni) and then LBE with 1008.1 ppmw Ni (LBE+1000Ni).

3.4. DOC-temperature measurements

After dissolving a portion of Ni in LBE, the starting temperature was set at 500 °C. To ensure that nickel begins to react with oxygen, the DOC was increased by EOP until a characteristic nucleation peak, different from PbO, was observed. Then, to attain and characterize equilibrium in the LBE, a steady-state DOC value was measured at a constant temperature selected in 200-500 °C with a step of 20-25 °C. The selected temperatures were not measured in a monotonous sequence, e.g. 350 °C, 300 °C, 475 °C and then 425 °C. If the measurements correspond to equilibrium, they must be independent of the side from which equilibrium is approached: during cooling (from 350 °C to 300 °C) or during heating (from 300 °C to 475 °C). Equilibrium was considered to have been reached when the average DOC value did not increase or decrease monotonically for at least 20-24 hours. The DOC trend was similar to that observed in [8]. Due to interruptions to the experiments, 3 points (375, 400, 425 °C at 1000 ppmw Ni added) were acquired after a shorter time (6-12 hours); however, they do not deviate from the measured trend and therefore these points are included in the final results. All equilibrium measurements are summarized in Table 1 and Fig. 2.

To characterize the kinetics in the LBE, a thermal cycling method was used to record the DOC as a function of temperature. This method assumes variation of the temperature while the total oxygen concentration remains unchanged, i.e. no external sources/sinks of oxygen other than chemical reactions in the LBE. Gradual cooling allows use to track the onset of chemical reactions in terms of DOC and temperature, while the following gradual heating forces these formed products to dissolve, returning the LBE to the initial state. When all the formed oxides have dissolved, the next thermal cycle starts at a slightly higher DOC, indicating the presence of a small but continuous oxygen in-leak from the ambient air into the setup. More details are provided in [7]. All thermal cycling tests in this study were conducted at the ramp rate of 0.5 °C/min, except for the tests in as-received LBE (1.0 °C/min). Fig. 3 summarizes all the thermal cycling tests. The tests in Fig. 3a (initial tests) and Fig. 3d (nucleation) were conducted in stirred LBE (200 rpm), while the tests in Fig. 3b (unknown oxide) and Fig. 3c (co-nucleation) were done in stagnant LBE.

The kinetics of NiO was measured in setup 2, LBE with 500.5 ppmw Ni added. At this nickel concentration, we were able to clearly measure the DOC for NiO nucleation, which occurred around 400 °C (Fig. 3d). In order to repeatedly measure the DOC for NiO nucleation, we had to heat up the LBE to 550 °C to completely dissolve the NiO formed. However, to measure the same at a lower nickel concentration (e.g.

in setup 1 with 203.2 ppmw Ni added), we would have to increase the DOC in the LBE. This is because we would need to compensate for the decrease in the dissolved nickel concentration in order to maintain the same driving force Eq. (12). This would require a temperature increase above 550 °C in setup 2, as the maximum DOC in LBE is limited by the oxygen saturation limit (Fig. 1). We preferred to avoid regular operation at temperatures above 550 °C and therefore focused only on setup 2.

3.5. Sampling of LBE

After all measurements, three samples (ca. 3-5 g each) were taken from setup 1 (LBE+200Ni) and then setup 2 (LBE+1000Ni) for inductively coupled plasma mass spectroscopy (ICP-MS) to validate complete Ni dissolution. Before sampling, we waited at least 14 h at 500 °C to ensure that all nickel compounds were dissolved in the LBE. Once the DOC had stabilized to a constant value, we changed the cover gas from N_2 to N_2+H_2 for at least 24 hours to reduce any oxides that might be floating on the gas-LBE interface. The DOC was well below the oxygen saturation limit at the time of sampling – below 10^{-6} wt.% DOC versus $8 \cdot 10^{-4}$ wt.% DOC at 500 °C.

Samples were taken from the LBE bulk in both setups – 1.5 cm from the bottom of the alumina crucible (total LBE height was ca. 7-8 cm). The sampling device consisted of a stainless steel tube closed at the bottom by a spring mechanism located inside the tube and regulated at the top of the tube. When the device was inserted into the LBE, pressing the mechanism opened the lower end and allowed the LBE to flow in. After releasing the mechanism to close the tube, the device was quickly removed from the setup and the sampled LBE was poured from the tube into a silicone mould to solidify. To change from one setup to the other, the sampling device was inserted into a batch of as-received LBE at 200 °C to clean it from the sampled LBE.

4 Results

4.1. Equilibrium measurements

Fig. 2 shows the steady-state measurements made in this paper. In Fig. 2, these measurements (markers) follow a consistent trend at each nickel level, with no sharp deviations. Furthermore, Appendix A4 shows a perfect reproducibility of these measurements by the DOC trends during the continuous heating of the LBE. This confirms the independence of the side from which the steady state was approached, i.e. after cooling (from 350 °C to 300 °C) or after heating the LBE (from 300 °C to 475 °C). These measurements therefore correspond to equilibrium. This reasoning is the same as in [5].

Table 1 summarize all the equilibrium measurements made in this paper. While the following subsections interpret these data in more detail, here we briefly describe their source in Table 1 (all calculations are explicitly written in an Excel file in the supplementary materials). The DOC and $ln\ a_O$ were calculated using Nernst's equation Eq. (13) from the measured temperature and potential difference. The activity of $Ni_{(lbe)}$ was calculated from the solubility product of NiO Eq. (8.1) using $ln\ a_O$. The activity coefficient of $Ni_{(lbe)}$ w.r.t. Ni(s) was derived from Eq. (9) based on $ln\ a_{Ni}$ and C_{Ni} as given in Table 1; the measurements at Bi_3Ni equilibrium were excluded because Bi_3Ni formation changes C_{Ni}. The activity of $Ni_{(lbe)}$ at equilibrium with Bi_3Ni was estimated by combining the derived $ln\ ^s\gamma_{Ni}$ and the low solubility limit Eq. (7.1).

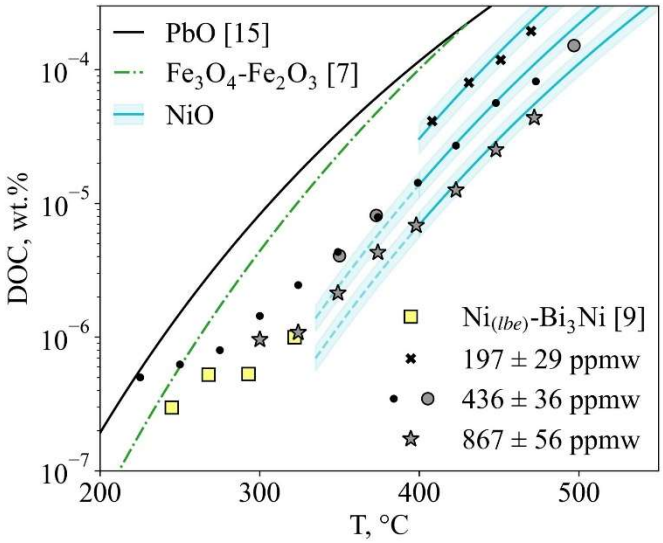

Figure 2. Measured NiO equilibrium at three Ni levels:

The *NiO* line is calculated from Eq. (10.1) for 197 ± 29, 436 ± 36 and 867 ± 56 ppmw Ni; the dashed lines extrapolate Eq. (10.1) below the temperature limit of S_{Ni} Eq. (7.2). The black markers represent our data acquired in stagnant conditions, the gray-filled markers represent our data acquired in stirred conditions (200 rpm).

First, we need to identify an oxide that forms in all the three LBE solutions, as indicated by the decreasing DOC values with temperature in Table 1. Using Eq. (11.1) and Eq. (11.2) we can identify whether this oxide is NiO or Fe_2NiO_4. To do this we use the measurements in LBE+200Ni and LBE+1000Ni to derive the ratio of C_{Ni} and the ratio of a_O.

Three samples were taken from LBE+200Ni and LBE+1000Ni, respectively, as described in section 3.5. The samples from LBE+200Ni contained on average 197 ± 29 ppmw Ni. The samples from LBE+1000Ni contained on average 867 ± 56 ppmw Ni. Their ratio is therefore 0.227 ± 0.037. Based on Table 1, the ratio of the a_O in LBE+1000Ni to the a_O in LBE+200Ni is 0.213 ± 0.039 in 398-472 °C[2]. These ratios satisfy Eq. (11.1), and therefore the oxide formed is NiO.

Now we can estimate the $Ni_{(lbe)}$ concentration in LBE+500Ni from the measurements in LBE+200Ni and LBE+1000Ni, since we did not measure it by a sampling technique. Using Eq. (11.1) we obtain 436 ± 36 ppmw Ni in LBE+500Ni.

For the sake of clarity, we rename the sets of data: 'LBE+200Ni' to 'LBE+197Ni', 'LBE+500Ni' to 'LBE+436Ni' and 'LBE+1000Ni' to 'LBE+867Ni'.

[2] To calculate the ratio of the a_O, two sets of values of $ln\ a_O$ were taken from Table 1 for LBE+200Ni and LBE+1000Ni in 398-472 °C respectively. Each set was fitted with the function $f(T) = A + B / T$. From these two obtained functions, we calculated the ratio of the a_O in LBE+1000Ni to the a_O in LBE+200Ni which is on average 0.213 ± 0.039.

Table 1. Equilibrium measurements. Reference states are Ni(s) and O_2(g) at 1 bar and 25 °C: all calculations are provided in an Excel file in the supplementary materials

T, °C	U, V	DOC, wt.%	ln a_O	ln a_{Ni}	ln $^s\gamma_{Ni}$, 1 / wt.%	ln a_{Ni} with Bi_3Ni
LBE+197Ni: C_{Ni} = 197 ± 29 ppmw, stagnant LBE						
470	0.720	$1.956 \cdot 10^{-4}$	-23.268	-4.543	-0.615 ± 0.147	0.513 ± 0.147 > 0
451	0.735	$1.191 \cdot 10^{-4}$	-24.338	-4.477	-0.550	0.294 > 0
431	0.746	$8.041 \cdot 10^{-5}$	-25.370	-4.562	-0.635	-0.107
408	0.764	$4.145 \cdot 10^{-5}$	-26.814	-4.484	-0.557	-0.415
LBE+436Ni: C_{Ni} = 436 ± 36 ppmw*, stagnant LBE**						
497*	0.729	$1.521 \cdot 10^{-4}$	-22.750	-3.717	-0.584 ± 0.083	0.925 ± 0.083 > 0
473	0.748	$8.204 \cdot 10^{-5}$	-24.048	-3.608	-0.476	0.697 > 0
448	0.758	$5.656 \cdot 10^{-5}$	-25.176	-3.803	-0.670	0.128 > 0
423	0.778	$2.721 \cdot 10^{-5}$	-26.719	-3.678	-0.545	-0.148
399	0.794	$1.430 \cdot 10^{-5}$	-28.198	-3.659	-0.527	-0.543
373*	0.806	$8.172 \cdot 10^{-6}$	-29.732	-3.830	-0.697	-1.196
374	0.807	$7.930 \cdot 10^{-6}$	-29.723	-3.770	-0.638	-1.117
350*	0.821	$4.070 \cdot 10^{-6}$	-31.359	-3.829	-0.696	-1.655
349	0.819	$4.354 \cdot 10^{-6}$	-31.334	-3.928	-0.795	-1.775
324	0.829	$2.457 \cdot 10^{-6}$	-33.002	-4.176	-1.043	-2.565
300	0.837	$1.445 \cdot 10^{-6}$	-34.675	-4.499	-1.366	-3.454
275**	0.845	$8.018 \cdot 10^{-7}$	-36.559	-4.880	-	-
250**	0.844	$6.271 \cdot 10^{-7}$	-38.225	-5.697	-	-
225**	0.842	$5.014 \cdot 10^{-7}$	-40.011	-6.642	-	-
LBE+867Ni: C_{Ni} = 867 ± 56 ppmw, stirred LBE						
472	0.768	$4.392 \cdot 10^{-5}$	-24.702	-3.005	-0.560 ± 0.065	0.598 ± 0.065 > 0
448	0.783	$2.530 \cdot 10^{-5}$	-25.981	-2.998	-0.553	0.245 > 0
423	0.801	$1.264 \cdot 10^{-5}$	-27.486	-2.911	-0.466	-0.069
398	0.815	$6.883 \cdot 10^{-6}$	-28.965	-2.955	-0.510	-0.545
374	0.824	$4.310 \cdot 10^{-6}$	-30.333	-3.161	-0.715	-1.195
349	0.838	$2.143 \cdot 10^{-6}$	-32.043	-3.219	-0.773	-1.754
324**	0.850	$1.086 \cdot 10^{-6}$	-33.818	-3.360	-	-
300**	0.847	$9.636 \cdot 10^{-7}$	-35.080	-4.094	-	-

* data acquired in LBE+436Ni with stirred LBE

** equilibrium with Bi_3Ni

*** estimated from the ratio of activity for LBE+197Ni and LBE+867Ni

4.2 NiO nucleation

4.2.1. As-received LBE

Prior to the addition of Ni in setup 2, a set of thermal cycling tests was conducted in the as-received LBE to screen its initial state (Fig. 3a). Every test was started at 450 °C, as this temperature was sufficient for complete dissolution of the oxides precipitated during cooling. As the thermal cycling tests show similar DOC trends, only one full thermal cycle is shown in Fig. 3a (initial test).

Analyzing the initial state of the as-received LBE (Fig. 3a), we note the following. On cooling from 400 °C (blue line), the DOC trend shows a continuous slight decrease until a characteristic drop due to Fe_2O_3. This slight decrease is thought to be mainly due to Reason (i) the propagation of uncertainty due to Sievert's

constant in Eq.(13) and Reason (ii) the influence of other unknown oxide formed at lower DOC [6]. However, this decrease is small compared to the DOC drops due to Fe_2O_3 and PbO and is therefore neglected. On subsequent heating from 200 °C (red line), we observe first the dissolution of PbO and then the dissolution of Fe_2O_3, both ending with a peak. The reason for the appearance of these two peaks is unclear, but their influence is considered minor as they disappear completely before 400 °C. After that, the DOC trend gradually increases and ends at a slightly higher value than the starting value due to the reverse effect of Reasons (i) and (ii), and a small continuous oxygen in-leak during the test.

4.2.2. NiO nucleation in the LBE bulk

After the Ni dissolution (LBE+436Ni), five thermal cycling tests were conducted at different DOC levels, as described in section 3.3 and 3.4 (Fig. 3d). In this case, each test was started at 550 °C to ensure complete dissolution of the nickel compounds formed during cooling. As we focus on the onset of NiO nucleation, only the cooling segments of the thermal cycles are plotted in Fig. 3d.

Analyzing the cooling segment in Fig. 3d, we note a significant DOC drop before Fe_2O_3 formation and PbO nucleation. This drop is caused by NiO, because if it were Fe_2NiO_4, it would only consume ca. $5.6 \cdot 10^{-6}$ wt.% DOC. This estimate is calculated from the stoichiometry of Eq. (1.2) and the Fe_2O_3 drop of ca. $1.4 \cdot 10^{-6}$ wt.% DOC in Fig. 3a (initial test), which corresponds to the Fe_3O_4 amount of $2.8 \cdot 10^{-6}$ wt.% DOC equivalent. Following the DOC trend further, we may see a slight drop due to Fe_2O_3 (just after the Fe_3O_4-Fe_2O_3 line) and then a drop due to PbO.

Similar to PbO [22], we can estimate the NiO nucleation limit at 500 ppmw Ni based on the onset points, which we define as the start of the monotonic decrease in the DOC trend for each cooling segment (nested figure in Fig. 3d).

4.2.3. NiO nucleation on the surface of PbO

As shown in Fig. 3d, NiO nucleation in the LBE bulk is improbable below 375 °C in the LBE with 436 ± 36 ppmw Ni. However, the energy barrier to nucleate on an existing surface should be lower than to create a new solid-liquid interface [21]. NiO nucleation may therefore still be possible on other precipitates already present in the LBE or formed on cooling, such as PbO. To evaluate this possibility, a thermal cycling tests were carried out under conditions that preclude NiO nucleation in the LBE bulk (Fig. 3b and Fig. 3c). These tests consisted of four thermal cycles in succession.

Only one thermal cycle is shown in Fig. 3b because the observed behavior was similar to the initial tests (Fig. 3a). This thermal cycle indicates the presence of another oxide which formed on cooling after Fe_2O_3 (between the vertical green arrows) but before PbO (around 10^{-6} wt.% and 210 °C) and which completely dissolved on heating. This oxide was not observed in the initial tests (Fig. 3a) and is therefore assumed to contain Ni in its composition, as it appeared after the addition of Ni to the LBE. The equilibrium of NiO and Fe_2NiO_4, Eq. (1.1) and Eq. (1.2), cannot explain the formation of this oxide. A working hypothesis is that this oxide is still Fe_2NiO_4, but it forms only after Fe_2O_3 formation has been triggered. Looking closely at Eq. (1.2), we can see that it requires a complex simultaneous exchange of electrons between $O_{(lbe)}$, $Ni_{(lbe)}$ and Fe_3O_4, which is formed by Fe^{2+} and Fe^{3+}. This reaction could consist of several steps including the Fe_3O_4-Fe_2O_3 reaction, which allows the change from Fe^{2+} to Fe^{3+}. However, at this stage, we leave this hypothesis for future research.

In Fig. 3c we show all the four thermal cycles, highlighting the first cooling segment and the last heating segment. The first cooling segment (blue line) has two DOC drops: as expected, the first drop due to Fe_2O_3

(between the vertical green arrows) and the second drop due to PbO[3] (after the DOC trend touches the PbO nucleation line). However, the subsequent heating segment ends at a lower value than the starting DOC. After four thermal cycles, the delta between the starting DOC and the final DOC reaches $2.0 \cdot 10^{-5}$ wt.%. This is different from the test in the as-received LBE (Fig. 3a) and therefore indicates incomplete dissolution of an oxide formed on cooling. As estimated in section 4.2.2, Fe_2NiO_4 would not be able to consume this DOC delta, which is about 3 times greater; hence this oxide is NiO.

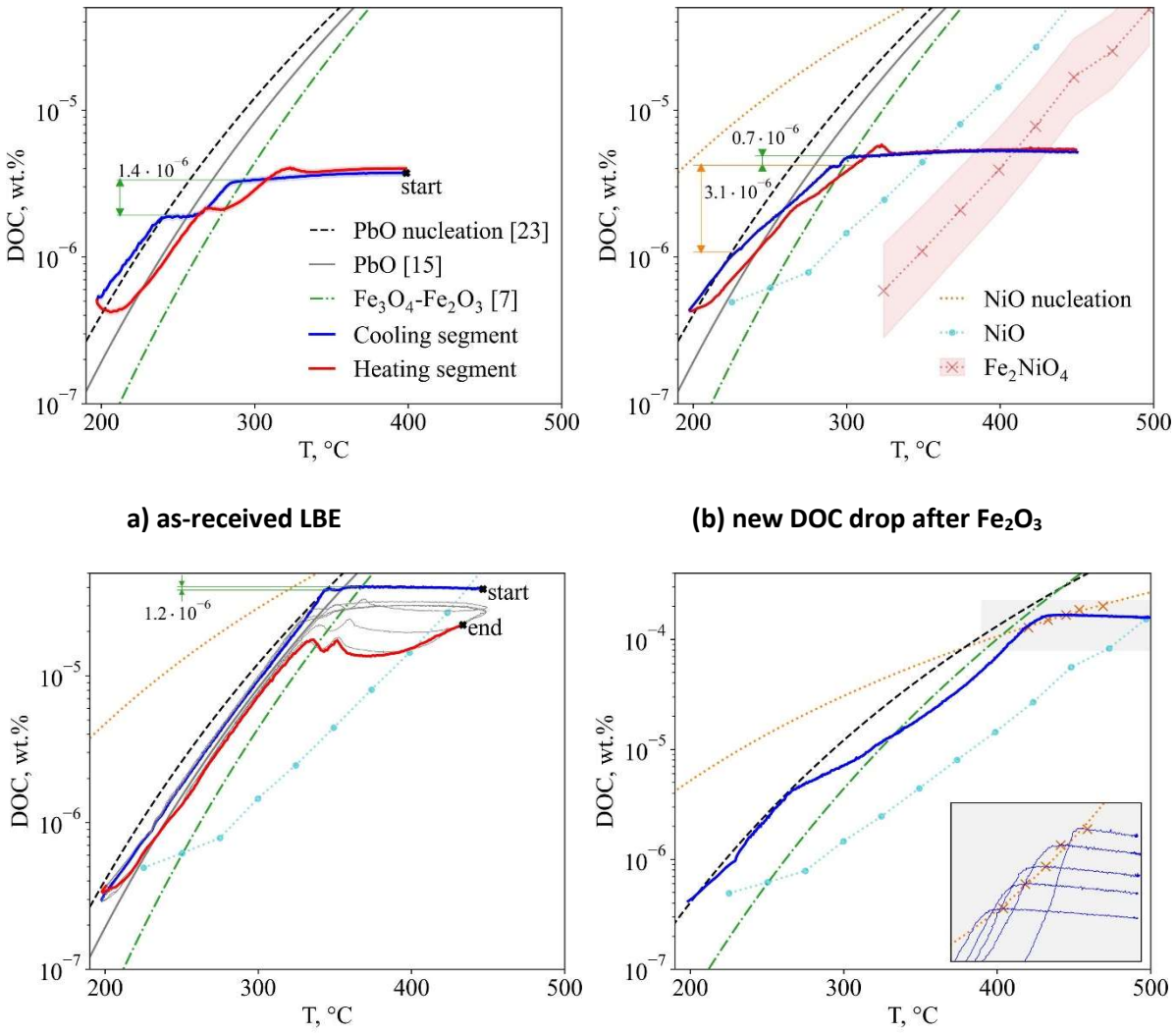

a) as-received LBE

(b) new DOC drop after Fe_2O_3

(c) NiO nucleation on PbO

(d) NiO nucleation in the LBE bulk

Figure 3. Thermal cycling tests in LBE+500Ni:

Fig. (a) shows a test in the as-received LBE, the other figures show tests in LBE+436Ni. The nested plot in Fig. (d) is in linear scale and it shows all cooling segments used to derive the *NiO nucleation* line (least-square fit by $ln\ DOC = a - b / T$). Each NiO onset point (brown cross) is defined as the start of the monotonic descent of a cooling segment. The NiO line represents our

[3] The second drop behaves slightly different from that in the other subfigures in Fig 3: the DOC only slightly touches the PbO nucleation line and then tends towards the PbO line. This is a typical behaviour of the DOC trend caused by the growth of nucleated PbO particles [22], explained in section 5.2.1.

equilibrium measurements in LBE+436Ni (Table 1). The Fe_2NiO_4 line is Eq.(10.2) but corrected on our γ_{Ni} (Table 1). The arrows indicate a DOC amount consumed by Fe_2O_3 (green arrows) and an unknown oxide (orange arrows).

5 Discussion

5.1. NiO equilibrium

5.1.1. Activity of Ni in LBE

In Fig. 2, below 325 °C the experimental data converge to one line which is in an agreement with the $Ni_{(lbe)}$-Bi_3Ni equilibrium data of [9]. In contrast, above 325 °C the experimental data consistently show a deviation from the predicted trend (*NiO* line) until 400 °C, above which the data and the predicted trend converge. As the S_{Ni} Eq. (7.2) was measured above 415 °C, this convergence is to be expected. However, the deviation between 325 °C and 400 °C is unexpected and is the subject of the following discussion.

As a result of the deviation, the DOC at 867 ppmw Ni (star markers) matches the predicted trend for 436 ppmw Ni in 325-375 °C, which would suggest a loss of ca. 420 ppmw Ni. Firstly, we cannot link this to the formation of a Bi-Ni intermetallic, as the DOC at 436 ppmw Ni (round markers) and 867 ppmw Ni (star markers) do not merge into one line. This is the case below 325 °C where the formation of solid Bi_3Ni limits the $Ni_{(lbe)}$ concentration and hence the DOC. Secondly, we cannot link this deviation to the formation of Fe_2NiO_4, as there is no sufficient source of Fe_3O_4 to consume 430 ppmw Ni Eq. (1.2). Therefore, we believe that this deviation corresponds to a change in the behavior of $Ni_{(lbe)}$ in the solution.

To quantify this deviation, we compare the partial Gibbs energy of Ni in LBE with the literature data for the Pb-Ni, Bi-Ni and LBE-Ni solutions. First, we derive ${}^{s}\gamma_{Ni}$ by combining Eq. (8.1) and Eq.(9), and then the partial Gibbs energy by combining Eq. (4) and Eq. (6). The ${}^{E}G_{Ni}$ of Pb-Ni, LBE-Ni and Bi-Ni were derived from the respective solubility data of Ni in Pb by *Alden et al. (1958)* as cited in [24], Ni in LBE [5] and Ni in Bi [26]. While the first two sets of solubility were measured directly, the latter was calculated by [26] from a thermodynamic assessment of the Bi-Ni binary by [25]. In Fig. 4, our ${}^{E}G_{Ni}$ values agree with each other regardless of the $Ni_{(lbe)}$ concentration, in accordance with Henry's law. They also reproduce the DOC trend of Fig. 2, where there is the deviation below 400 °C.

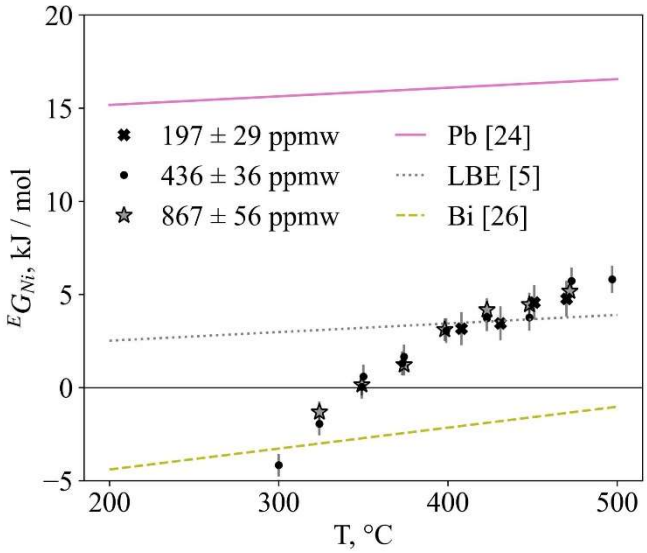

Figure 4. Partial excess Gibbs free energy of Ni in Pb-Ni, Bi-Ni and LBE-Ni solutions:

The ${}^{E}G_{Ni}$ functions (*Pb*, *LBE*, and *Bi* lines)are derived based on the literature data. The markers represent our experimental data obtained in three solutions of LBE with different levels of Ni recalculated for the reference state of pure liquid nickel.

For a solution of A and B, if ${}^{E}G_{m} > 0$ then A and B tend to de-mix, i.e. the atoms prefer to interact with their own kind (A-A and B-B interactions) [14]. In practice this results in a miscibility gap, as in the Pb-Ni system [27]. In contrast, when ${}^{E}G_{m} < 0$, the atoms prefer to interact with the opposite kind (A-B interactions). This is often indicated by the presence of intermetallics, e.g. Bi_3Ni and BiNi in the Bi-Ni system [25]. Since LBE is ca. 55 % Bi and 45 % Pb, the behavior of $Ni_{(lbe)}$ in LBE is believed to be an 'average' of these two binaries. Considering the formation of Bi_3Ni detected in LBE [5, 13], the behavior of $Ni_{(lbe)}$ in LBE must be close to that in pure Bi. Thus, the observed deviation of ${}^{E}G_{Ni}$ towards ${}^{E}G_{Ni}$ in pure Bi is theoretically reasonable.

To place our measured γ_{Ni} in the context of data from the literature [5,9], we construct a plot of the $Ni_{(lbe)}$ activity as a function of temperature when Bi_3Ni is stable (Fig. 5). This plot is also known as the van 't Hoff plot [28]. It is convenient here to calculate the $Ni_{(lbe)}$ activity w.r.t. pure Ni(s) using Eq.(9), so that $a_{Ni} = 1$ when $Ni_{(lbe)}$ reaches the equilibrium with Ni(s). The $Ni_{(lbe)}$ concentration in Eq. (9) is the low-temperature solubility limit Eq. (7.1).

We have two options for γ_{Ni} for Eq. (9). The first option comes from [5], Eq. (5) and Eq. (7.2), which we used in the solubility product Eq. (10.1) and Eq. (10.2). The second option comes from our measurements (Table 1). In Fig. 5, the *[5]* line represents the former, while the *[5] + this study* markers correspond to the latter. Below 325 °C, we and [9] measured a_O directly at the equilibrium of NiO with Bi_3Ni. Our measured values are converted directly to a_{Ni} via Eq. (8.1).

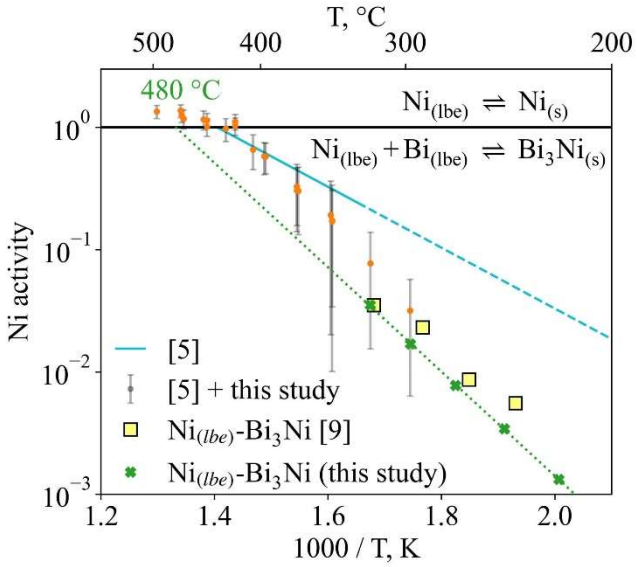

Figure 5. Activity of Ni in LBE:

The activity ([5]) line was calculated combining Eq. (5), Eq. (7.1), Eq. (7.2) and Eq. (9). The *[5] + this study* markers are given in Table 1. *This study* markers are calculated directly via Eq. (8.1) from the oxygen activity measurements.

In Fig. 5, below the unity threshold (*a = 1)*, the values calculated from Eq. (7.1) and our γ_{Ni} values (*[5] + this study*) form approximately one line with the region of Bi_3Ni. According to the van 't Hoff equation, the slope of a line in these coordinates can be linked to the equilibrium constant of the corresponding reaction [28]. Since the line in Fig. 5 has only one slope, we assume that it represents only one continuous

equilibrium, which in our case is the Bi_3Ni equilibrium. Furthermore, a straight line through our data when Bi_3Ni is in LBE – the *$Ni_{(lbe)}$-Bi_3Ni (this study)* markers – crosses the unity threshold at ca. 480 °C, which is close to the melting point of Bi_3Ni – 471 °C [12]. We therefore exclude the formation of BiNi in LBE below ca. 470 °C. This conclusion is in good agreement with the experimental observations of [5], in which the authors identified only two regions limiting the $Ni_{(lbe)}$ concentration: Bi_3Ni formation and Ni(s) formation. Moreover, this agreement obtained between the independently measured data by [5] and [9] is considered to validate the γ_{Ni} values obtained in our study.

5.1.2. Gibbs energy of Bi_3Ni formation

Finally, we derive the Gibbs energy of formation of Bi_3Ni $\Delta_f°G_{Bi3Ni}$ from our measurements (Table 1) combined with Eq.(7.1) of [5] and the measurements of [9] (Fig. 6). We base our calculations on equilibrium Eq. (14.1) described by Eq. (14.2)

$$3\ Bi(lbe) + Ni(lbe) = Bi_3Ni(s) \qquad (14.1)$$

$$\Delta_f°G_{Bi3Ni} = RT \ln {}^{s}a_{Ni(lbe)} + 3\ RT \ln {}^{s}a_{Bi(lbe)} \qquad (14.2)$$

with ${}^{s}a_{Ni(lbe)}$ and ${}^{s}a_{Bi(lbe)}$ the activity of $Ni_{(lbe)}$ and $Bi_{(lbe)}$ w.r.t. Ni(s) and Bi(rhomb), respectively. We calculated an expression for $a_{Bi(lbe)}$ from the activity of $Bi_{(lbe)}$ w.r.t. pure liquid Bi by [19] with [29] data (Appendix A2).

There are various thermodynamic assessments of the Bi-Ni binary providing different values of $\Delta_f°G_{Bi3Ni}$ [25, 30-35]. The most recent was performed in [35] taking into account the calorimetric measurements of BiNi and Bi_3Ni [12, 36]. To the best of our knowledge, the calorimetric measurements of [12, 36] are the only experimental measurements of Bi_3Ni formation to date. Fig. 6 compares our calculations and these calorimetric measurements with several assessed functions of $\Delta_f°G_{Bi3Ni}$. The large scatter in Fig. 6 shows that there is no agreement on $\Delta_f°G_{Bi3Ni}$ data in the literature. Our data are far from the calorimetric data, but close to the data from thermodynamic assessments. At the moment it is impossible to locate the region of the true values of $\Delta_f°G_{Bi3Ni}$. More measurements are therefore needed.

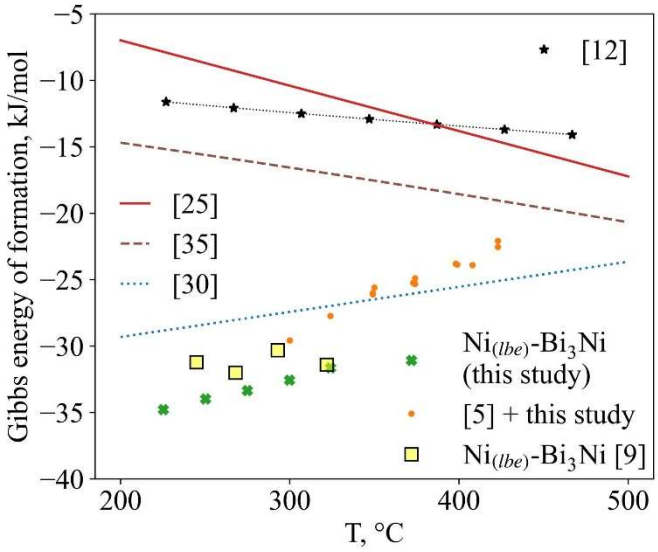

Figure 6. Gibbs energy of formation of Bi_3Ni:

The reference states for all values of $\Delta_f°G_{Bi3Ni}$ are Bi(rhomb) and Ni(s). The lines represent assessed data. The markers represent experimental data. The *[5] + this study* markers were calculated from Eq.(14.2) using the nickel concentration in the presence of

Bi_3Ni Eq.(7.1) [5] and the activity coefficient determined in this work (Table 1). The *$Ni_{(lbe)}$-Bi_3Ni [9]* markers were taken from [9]. The *$Ni_{(lbe)}$-Bi_3Ni (this study)* markers were calculated via Eq.(14.2) and Eq.(8.1) from the oxygen activity measurements.

5.2. Conditions for NiO nucleation

5.2.1. NiO nucleation in the LBE bulk

Based on the classical nucleation theory, a certain supersaturation is needed to overcome the energy barrier associated with the formation of a new solid-liquid interface, known as "nucleation barrier" [21]. Once the nucleation barrier is overcome, particles nucleate and continue to grow consuming the available reagents until equilibrium is reached. In the case of PbO in LBE, the driving force Eq. (12) reduces to a function of the ratio of the DOC to the equilibrium oxygen concentration at a given temperature. When this ratio, known as 'oversaturation', reaches a certain value, PbO begins to nucleate, defining the PbO nucleation limit in LBE [22]. Newly nucleated PbO particles rapidly consume the DOC, bringing the system to the PbO equilibrium (the oxygen saturation limit). Since NiO is assumed to form from the dissolved species in Eq. (1.1), we expect a similar behavior: a nucleation limit and then equilibrium.

Extrapolation of the obtained NiO nucleation limit to low temperatures indicates a DOC much higher than the PbO nucleation limit, which is therefore impossible to exceed (Fig. 3d). Given the theory in section 2.4, we expect that the bulk NiO nucleation at low $Ni_{(lbe)}$ concentration is impossible, as it would require even lower temperatures/higher DOC compared to the test conditions. Furthermore, the DOC trend failed to reach the NiO equilibrium before Bi_3Ni formation below ca. 275 °C, suggesting a slow growth of the nucleated NiO particles under these conditions.

5.2.2. NiO nucleation on the surface of PbO

The data in Fig. 3a show that PbO and Fe_2O_3 are completely dissolved at 50 °C above their equilibrium temperatures. In contrast, in Fig. 3c we observe that once PbO and Fe_2O_3 are dissolved (two small peaks), there is still a slight DOC consumption followed by a DOC increase after crossing the NiO equilibrium. This suggests that PbO triggered the nucleation of NiO, which grew slowly at temperatures below the NiO equilibrium and began to dissolve as LBE was heated above the NiO equilibrium.

In two other thermal cycles with lower starting DOC (Fig. 3b), all oxides dissolve completely on heating and a DOC increment due to an oxygen in-leak becomes visible, as in Fig. 3a (the initial test). These two tests confirm that the amount of PbO formed, and therefore the total amount of precipitates in the LBE, is an important factor influencing NiO nucleation. In this particular example, an amount of PbO equivalent to ca. $4.0 \cdot 10^{-5}$ wt.% DOC in Fig. 3c is sufficient to cause NiO formation, whereas $1.0 \cdot 10^{-6}$ wt.% DOC in Fig. 3b is not. Such amounts are unachievable in the normal operation of the MYRRHA, in which the DOC is controlled below 10^{-6} wt.%.

Conclusion

In the present study, we have experimentally characterized the thermodynamic stability and nucleation behavior of NiO in liquid lead-bismuth eutectic (LBE) at elevated nickel concentrations.

Regarding the NiO stability, the DOC trend measured at three different Ni levels in LBE followed well the literature-based thermodynamic calculations above 400 °C and the literature experimental data below 325 °C. The activity coefficient of Ni in LBE was derived from the measured data at the intermediate temperatures. Finally, the Gibbs energy of Bi_3Ni formation was estimated from the available experimental measurements in LBE.

Regarding the NiO nucleation, the thermal cycling tests revealed two cases. In the case of NiO nucleation in the LBE bulk, NiO required a significant DOC above the NiO equilibrium. In the case of NiO nucleation on the surface of PbO, NiO required a large fraction of PbO. Based on these observations, we concluded that NiO was unlikely to form under the MYRRHA operating conditions.

Appendixes

A1. Correlation between the activity coefficient and solubility data

There are no direct measurements of the activity coefficient of Ni in LBE in the literature. Two options are considered to derive this parameter. The first option is to calculate it from a comprehensive thermodynamic assessment of a system including all phases in the LBE-O-Ni system. The second option is to use solubility data of Ni in LBE, since Henry's law is valid for high dilutions of Ni in LBE. These two options are compared in this appendix.

The second option is based on the solubility data measured at equilibrium Eq. (A3.1) between dissolved nickel Ni(lbe) and solid nickel Ni(FCC), or Ni(s), above 400 °C, when there is no intermetallic phase according to [5, 17]. At equilibrium the chemical potentials of these two phases are equal Eq. (A1.2).

$$Ni(lbe) \leftrightarrow Ni(s) \tag{A1.1}$$

$$\mu_{Ni(lbe)} = \mu_{Ni(s)} \tag{A1.2}$$

By definition, the chemical potential of species *X* is the sum of a reference state contribution μ° and the excess mixing contribution *RT ln a*, with *a* the chemical activity of species *X* in the solution [14]. Assuming the solid FCC_A1 phase as a reference state for Ni(s) [16], we arrive to Eq. (A1.3).

$$\mu^{\circ}{}_{Ni(FCC)} + RT \ln a = \mu^{\circ}{}_{Ni(FCC)} \tag{A1.3}$$

In a dilute solution, Ni obeys Henry's law, therefore the chemical activity *a* is a product of the dissolved nickel concentration *C* and the activity coefficient *γ*. Since we consider the equilibrium with the pure solid nickel, the dissolved nickel concentration *C* is equal to the solubility of Ni in LBE, *S* from Eq. (7.2). Therefore, Eq. (A1.3) yields Eq. (A1.4) and then Eq. (A1.5).

$$\mu^{\circ}{}_{Ni(FCC)} + RT \ln \gamma + RT \ln S = \mu^{\circ}{}_{Ni(FCC)} \tag{A1.4}$$

$$\ln \gamma \cdot S = 0 \tag{A1.5}$$

From Eq. (A1.5), the activity coefficient *γ* is therefore the reciprocal of the solubility *S*, Eq. (A1.6).

$$\ln \gamma = -\ln S \tag{A1.6}$$

To demonstrate the accuracy of Eq. (A1.6), we provide the following comparison in Fig. A1.1. We take the thermodynamic assessment from [26], which incorporates the solubility data Eq. (7.2) of [5]. Using this thermodynamic assessment, we calculate equilibrium Eq. (A1.1) in 200-1000 °C, from which we derive the activity coefficient of Ni in LBE (black dashed line). For comparison, we assume Henry's law for Ni in LBE and take the high-temperature solubility correlation from the same thermodynamic assessment [26] to

derive the activity coefficient via Eq. (A1.6). This is shown as a red solid line, which is extrapolated down to lower temperatures (red dotted line).

Modelling the equilibrium Eq. (A1.1) below 400 °C is not realistic, because Bi_3Ni forms instead of Ni(s) at lower temperatures. However, it allows us to compare how accurate is the Henry's law assumption in comparison to complete thermodynamic assessment. As we may see, the values of these two lines are 2 times different at 200 °C. We consider this deviation to be tolerable for the calculation of NiO equilibrium. Therefore, instead of full thermodynamic assessment of a system including LBE, Ni, O and NiO, we use the activity coefficient from the direct solubility measurement.

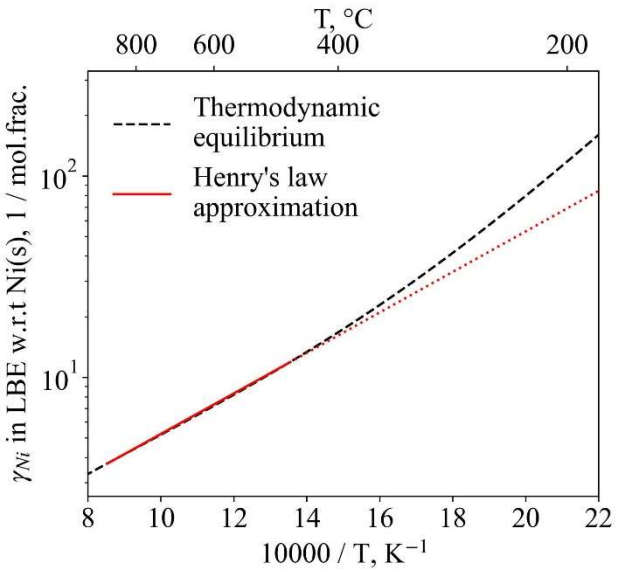

Figure A1.1. Comparison of the activity coefficient obtained from thermodynamic equilibrium modelling based on [26] and from extrapolation of the high-temperature solubility law of [26].

A2. Reference state change

The chemical potential, or the partial Gibbs free energy, is defined with respect to a selected reference state [14]. For example, the chemical potential of Bi in LBE can be defined w.r.t. pure Bi(rhomb), denoted as Bi(s) in Eq. (A2.1). However, regardless of a chosen reference state, the value of the chemical potential $\mu_{Bi(lbe)}$ must remain the same. Therefore, depending on the reference state, the value of the activity, specifically the activity coefficient, must change. Equations below derive a change from Bi(s) to pure liquid Bi(l).

$$\mu_{Bi(lbe)} = {}^\circ\mu_{Bi(s)} + RT \ln a_{Bi(lbe)} \qquad (A2.1)$$

$${}^\circ\mu_{Bi(l)} + RT \ln \tilde{a}_{Bi(lbe)} = \mu_{Bi(lbe)} = {}^\circ\mu_{Bi(s)} + RT \ln a_{Bi(lbe)}$$

$$\ln a_{Bi(lbe)} = \ln \tilde{a}_{Bi(lbe)} + ({}^\circ\mu_{Bi(l)} - {}^\circ\mu_{Bi(s)}) / RT \qquad (A2.2)$$

with ${}^\circ\mu_{Bi(s)}$ and ${}^\circ\mu_{Bi(l)}$ the (standard-state) chemical potential of Bi(s) and Bi(l), respectively ($J \cdot mol^{-1}$); $a_{Bi(lbe)}$ and $\tilde{a}_{Bi(lbe)}$ the activity of Bi w.r.t. Bi(s) and Bi(l), respectively, R the gas constant (8.3145 $J \cdot mol^{-1} \cdot K^{-1}$) and *T* temperature in Kelvin. Functions of ${}^\circ\mu_{Bi(s)}$ and ${}^\circ\mu_{Bi(l)}$ are given in [16]: *RHOMBO_A7* for Bi(s) and *LIQUID* for Bi(l). The function of $\tilde{a}_{Bi(lbe)}$ is calculated by [19] using the correlations of [29].

Plugging $^{\circ}\mu_{Bi(s)}$, $^{\circ}\mu_{Bi(l)}$ and $\tilde{a}_{Bi(lbe)}$ data into Eq. (A2.2), values of ln $a_{Bi(lbe)}$ were calculated for each 0.01 °C in the range 200-500 °C. These values were fitted with $\log_{10} a_{Bi(lbe)} = A + B / T$ to define a convenient expression, Eq. (A2.3). The uncertainty of the fit is less than 0.01 %.

$$\log_{10} a_{Bi(lbe)} = -1.3532 + 546.7076 / T[K] \qquad \text{(A2.3)}$$

A3. Neutron activation analysis of as-received LBE

An LBE sample was taken at 200 °C from setup 1 after skimming off the oxides from the surface of the LBE. The sampled LBE was solidified and re-melted into a cylindrical shape (approx. 3 cm length and 5 mm diameter) for the needs of neutron activation analysis (NAA). The analysis was performed at SCK CEN. The results are shown in Table A3.1.

Table A3.1. Impurity composition of as-received LBE sampled at 200 °C by NAA (selected elements).

	µg/g		µg/g
Ag	16.8 ± 0.8	Fe	< 1.5
Cu	15.8 ± 1.1	Cr	< 0.03
Al	7.68 ± 0.36	Mn	< 0.005
Ni	< 15	Co	< 0.004

In Table 1, the aluminium concentration is sufficiently high, 7.68 ± 0.36 ppmw. All this amount is expected to be in the form of α-Al_2O_3 due to its high thermodynamic stability [19]. According to the Ellingham diagram [19], Al_2O_3 can also react with dissolved nickel following Eq. (A3.1).

$$Ni(lbe) + O(lbe) + \alpha\text{-}Al_2O_3(s) = NiAl_2O_4(s) \qquad \text{(A3.1)}$$

As the NiO reaction Eq. (1.1), the $NiAl_2O_4$ reaction Eq. (A3.1) also follows the stoichiometric condition Eq. (11.1). However, equilibrium calculations can help to distinguish between NiO and $NiAl_2O_4$ in the same way as between NiO and Fe_2NiO_4 in Fig. 1.

At equilibrium, the $NiAl_2O_4$ reaction Eq. (A3.1) obeys the law of mass action, expressed by Eq. (A3.2). Using Henry's law Eq. (9), the equilibrium constant can be expressed in terms of concentration, Eq. (A3.3).

$$\Delta_r{}^{\circ}G = RT \ln(a_{Ni} \cdot a_O) \qquad \text{(A3.2)}$$

$$\Delta_r{}^{\circ}G = RT \ln({}^{s}\gamma_{Ni} \cdot C_{Ni} \cdot k_S \cdot C_O)$$

$$\ln(C_{Ni} \cdot C_O) = \frac{\Delta_r{}^{\circ}G}{RT} - \ln {}^{s}\gamma_{Ni} - \ln k_S$$

$$\ln(C_{Ni} \cdot C_O) = 6.23 - \frac{15297}{T\,[\mathrm{K}]} \qquad \text{(A3.3)}$$

with $\Delta_r{}^{\circ}G\ [\mathrm{kJ/mol}] = -486.53 + 0.158 \cdot T\ [\mathrm{K}]$ from [19], the activity coefficient ${}^{s}\gamma_{Ni}$ is defined by Eq. (5) with the solubility data Eq. (7.2) and Sievert's constant k_S is defined by $\log_{10} k_S \left[\frac{1}{\mathrm{wt}}.\%\right] = 3.12 - 7072/T\ [\mathrm{K}]$ from [15].

Fig. A3.1 compares the $NiAl_2O_4$ equilibrium Eq. (A3.3), the calculated NiO equilibrium Eq. (10.1) and the measured DOC at equilibrium in setup 1 with 197 ± 29 ppmw of Ni. The two lines (*NiO* and *$NiAl_2O_4$*), are

sufficiently well apart, e.g. the DOC of the NiO equilibrium is eight times higher than the DOC of the $NiAl_2O_4$ equilibrium at 415 °C. Therefore, the measured values clearly indicate that the oxide at equilibrium is NiO.

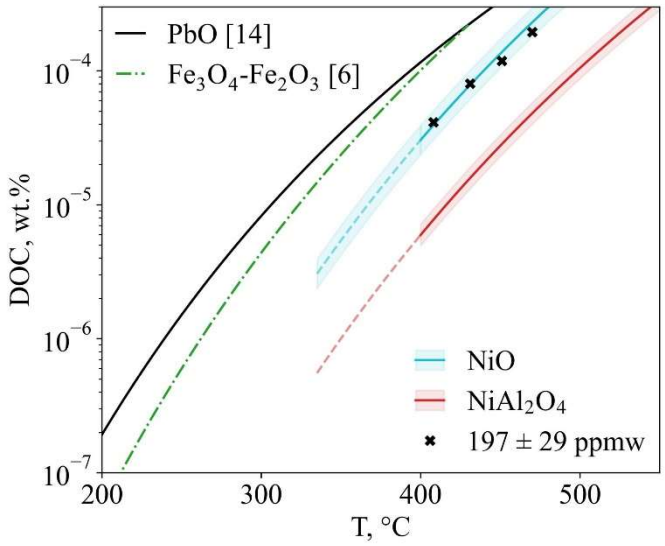

Figure A3.1. Calculated equilibrium of NiO and $NiAl_2O_4$ and measurements at 197 ± 29 ppmw Ni in LBE: The *NiO* and *$NiAl_2O_4$* lines are calculated from Eq. (10.1) and Eq. (A3.3), respectively, for 197 ± 29 ppmw Ni. The dashed lines extrapolate Eq. (10.1) and Eq. (A3.3) below the temperature limit of S_{Ni} Eq. (7.2). The markers represent our data acquired in setup 1 at 197 ± 29 ppmw Ni (Table 1).

A4. Reproducibility of equilibrium measurements

In [5] the authors demonstrated the independence of their measurements from the type of experiment, i.e. “increasing temperature ramp” or “decreasing temperature rate”. This confirmed the equilibrium state and therefore the reliability of their solubility measurements. In our experiments, we followed the same approach, as described in section 3.4. Some of the steady-state measurements were taken after cooling of the LBE (“decreasing temperature ramp”) and some of them were taken after heating of the LBE (“increasing temperature ramp”). In addition, a DOC trend was measured during continuous heating of the LBE (heating segment in Fig. A4.1) for comparison with the steady-state measurements. In Fig. A4.1, all measurements follow the same trends at their respective nickel levels, confirming the equilibrium state.

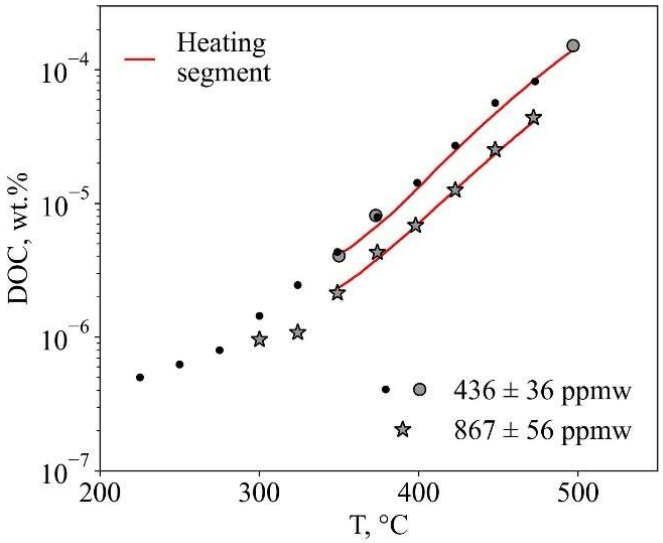

Figure A4.1. Reproducibility of equilibrium measurements:

The markers correspond to the steady-state measurements in LBE with 436 ± 36 ppmw Ni and LBE with 867 ± 56 ppmw Ni respectively. The black markers represent our data acquired in stagnant conditions, the gray-filled markers represent our data acquired in stirred conditions (200 rpm). Heating segments were acquired during continuous heating of LBE for both nickel levels; cooling rate was below 0.5 °C/min, stirred conditions (200 rpm).

References

1. H. Aït Abderrahim, P. Baeten, D. De Bruyn, R. Fernandez, MYRRHA – A multi-purpose fast spectrum research reactor, Energy Conversion and Management. 63 (2012) 4–10. https://doi.org/10.1016/j.enconman.2012.02.025
2. J. Zhang, N. Li, Review of the studies on fundamental issues in lbe corrosion. J. Nucl. Mater. 73 (2008) 351–377. http://dx.doi.org/10.1016/j.jnucmat.2007.06.019.
3. B. Gromov, Y. Belomitcev, E. Yefimov, M. Leonchuk, P. Martinov, Y. Orlov, D. Pankratov, Y. Pashkin, G. Toshinsky, V. Chekunov, B. Shmatko, V. Stepanov, Use of lead-bismuth coolant in nuclear reactors and accelerator-driven systems. J. Nucl. Mater. 173 (1997) 207–217. http://dx.doi.org/10.1016/S0029-5493(97)00110-6.
4. V. Tsisar, C. Schroer, O. Wedemeyer, A. Skrypnik, J. Konys, Long-term corrosion of austenitic steels in flowing LBE at 400 °C and 10^{-7} mass% dissolved oxygen in comparison with 450 and 550 °C. J. Nucl. Mater. 468 (2016) 305-312. https://doi.org/10.1016/j.jnucmat.2015.09.027.
5. L. Martinelli, F. Vanneroy, J.C. Diaz Rosado, D. L'Hermite, M. Tabarant, Nickel solubility limit in liquid lead–bismuth eutectic. J. Nucl. Mater. 400 (2010) 232–239. http://dx.doi.org/10.1016/j.jnucmat.2010.03.008.
6. A. Aerts, S. Gavrilov, G. Manfredi, A. Marino, K. Rosseel, J. Lim, Oxygen–iron interaction in liquid lead–bismuth eutectic alloy, Physical Chemistry Chemical Physics. 18 (2016) 19526-19530. https://doi.org/10.1039/C3cP01561A
7. A. Tsybanev, K. Gladinez, J. Lim, A. Marino, N. Moelans, A. Aerts, Identification of the Fe_3O_4-Fe_2O_3 reaction in liquid lead-bismuth eutectic, Progress in Nuclear Energy. 164 (2023) 104884. https://doi.org/10.1016/j.pnucene.2023.104884

8. G. Gregori, T. Doneux, J. Lim, Electrochemical Measurement of CoO Solubility Product and Co Solubility in Molten Lead-Bismuth Eutectic by Solid-State Ionic Devices. J. Electrochem. Society. 170 (2023) 061505. https://doi.org/10.1149/1945-7111/acdc56.
9. G. Gregori, V. Tsisar, T. Doneux, J. Lim, Electrochemical and metallographic characterization of Ni-NiO-NiBi3 equilibrium in molten lead-bismuth eutectic. J. Nucl. Mater. 589 (2024) 154866. https://doi.org/10.1016/j.jnucmat.2023.154866.
10. OECD NEA, Chemical Thermodynamics of Nickel, Chemical Thermodynamics Volume 6, OECD Publishing, Paris, 2020. https://www.oecd-nea.org/jcms/pl_37415/chemical-thermodynamics-of-nickel
11. G. Gregori, A. Aerts, K. Gladinez, K. Rosseel, T. Doneux, J. Lim, Electrochemical measurement of solubility product of metal oxides in liquid metals by coulometric titration of oxygen, Electrochimica Acta. 432 (2022) 141202. https://doi.org/10.1016/j.electacta.2022.141202
12. R. Agarwal, P. Samui, S.G. Kulkarni, Thermodynamic investigations of (Bi + Ni) system – Part II, J. Chem. Thermodynamics. 57 (2013) 477-484. http://dx.doi.org/10.1016/j.jct.2012.09.010
13. C. Schroer, O. Wedemeyer, V. Tsisar, A. Skrypnik, J. Konys, Practical experience gained from operating the lead-bismuth loop CORRIDA, in: Proceedings of the 26th International Conference on Nuclear Engineering (ICONE26), London, UK, 2018. July 22nd -26th. https://scholar.archive.org/work/xpunxuqn2jbx5bvkmdik2s4ux4/access/wayback/https://publikationen.bibliothek.kit.edu/1000084968/15952086
14. M. Hillert, Phase Equilibria, Phase Diagrams and Phase Transformations, Second Edition, Cambridge University Press, 2008.
15. J. Lim, G. Manfredi, A. Marino, K. Gladinez, A. Aerts, Electrochemical measurement of sieverts' constant and solubility of oxygen in LBE at 598–748 K, Journal of the Electrochemical Society. 164 (2017) H743–H747. http://dx.doi.org/10.1149/2.0231712jes
16. A.T. Dinsdale, SGTE data for pure elements, Calphad. 15 (1991) 317-425. https://doi.org/10.1016/0364-5916(91)90030-N
17. P.N. Martynov, K.D. Ivanov, in: Proceedings of Four Technical Meeting Held Between December 1995 and April 1998, 1998, pp. 177–184.
18. OECD NEA, Chemical Thermodynamics of Iron, Part 1, Chemical Thermodynamics Volume 13a, OECD Publishing, Paris, 2013. https://www.oecd-nea.org/jcms/pl_14374/chemical-thermodynamics-of-iron-part-1?details=true
19. C. Schroer, J. Konys. Physical Chemistry of Corrosion and Oxygen Control in Liquid Lead and Lead-Bismuth Eutectic. 2007. https://publikationen.bibliothek.kit.edu/270069895
20. N. Rimbert, L. Claudotte, P. Gardin, J. Lehmann, Modeling the Dynamics of Precipitation and Agglomeration of Oxide Inclusions in Liquid Steel. Ind. Eng. Chem. Res., 53 (2014) 8630–8639. https://pubs.acs.org/doi/10.1021/ie403991e
21. V. Kalikmanov, Nucleation Theory, volume 860 of Lecture Notes in Physics, Springer, 2013.
22. K. Gladinez, K. Rosseel, L. Lim, A. Marino, G. Heynderickx, A. Aerts, Nucleation and growth of lead oxide particles in liquid lead-bismuth eutectic, Phys. Chem. Chem. Phys. 19 (2017) 27593–27602. http://dx.doi.org/10.1039/C7CP05068B
23. K. Gladinez, K. Rosseel, J. Lim, A. Marino, G. Heynderickx, A. Aerts, Formation and transport of lead oxide in a non-isothermal lead-bismuth eutectic loop, Nuclear Engineering and Design. 349 (2019) 78-85. https://doi.org/10.1016/j.nucengdes.2019.04.021
24. OECD NEA, Handbook on Lead-bismuth Eutectic Alloy and Lead Properties, Materials Compatibility, Thermal-hydraulics and Technologies, NEA No. 7268, Nuclear Energy Agency OECD,

Paris, 2015. https://www.oecd-nea.org/jcms/pl_14972/handbook-on-lead-bismuth-eutectic-alloy-and-lead-properties-materials-compatibility-thermal-hydraulics-and-technologies-2015-edition?details=true

25. G. Vassilev, V. Gandova, P. Docheva, Comments and reconciliation of the Ni–Bi-system thermodynamic reassessments, Cryst. Res. Technol. 44 (2009) 25-30. https://doi.org/10.1002/crat.200800391
26. S. Gosse, Thermodynamic assessment of solubility and activity of iron, chromium, and nickel in lead bismuth eutectic, Journal of Nuclear Materials. 449 (2014) 122-131. http://dx.doi.org/10.1016/j.jnucmat.2014.03.011
27. I. Kainulainen, P. Taskinen, J. Gisby, A thermodynamic assessment of the nickel–lead system, CALPHAD: Computer Coupling of Phase Diagrams and Thermochemistry. 34 (2010) 441-445. http://dx.doi.org/10.1016/j.calphad.2010.08.001
28. P. Atkins and J. De Paula, Physical Chemistry, Ninth edition, W.H. Freeman and Company, 2010.
29. N.A. Gokcen, The Bi-Pb (Bismuth-Lead) System, Journal of Phase Equilibria. 13 (1992) 21-32. https://doi.org/10.1007/BF02645372
30. G.P. Vassilev, X.J. Liu, K. Ishida, Experimental Studies and Thermodynamic Optimization of the Ni-Bi System, Journal of Phase Equilibria and Diffusion. 26 (2005) 161-168. https://doi.org/10.1007/s11669-005-0134-0
31. G.P. Vassilev, J. Romanowska, G. Wnuk, Bismuth activity measurements and thermodynamic re-optimization of the Ni –Bi System, Int. J. Mat. Res. 98 (2007) 468-475. https://doi.org/10.3139/146.101499
32. J. Wang, F. Meng, L. Liu, Z. Jin, Thermodynamic optimization of Bi-Ni binary system, Transactions of Nonferrous Metals Society of China. 21 (2011) 139-145. https://doi.org/10.1016/S1003-6326(11)60690-0
33. Y. Liu, S. Liu, C. Zhang, X. Lu, C. Chen, Y. Du, D. Zivkovic, Thermodynamic Assessment of the Bi–Ni and Bi–Ni–X (X = Ag, Cu) Systems, J. Electron. Mater. 45 (2016) 1041–1056. https://doi.org/10.1007/s11664-015-4272-9
34. S.-K. Seo, M.G. Cho, H.M. Lee, Thermodynamic Assessment of the Ni-Bi Binary System and Phase Equilibria of the Sn-Bi-Ni Ternary System, J. of Electronic Materials. 36 (2007) 1536-1544. https://doi.org/10.1007/s11664-007-0256-8
35. P. Samui, R. Agarwal, Thermodynamic assessment and solubility of Ni in LBE coolants, Thermo 2 (2022) 371–382, https://doi.org/10.3390/thermo2040025.
36. P. Samui, R. Agarwal, A.P.S.G. Kulkrani, Thermodynamic investigation of Bi-Ni system – Part I, J. Chem. Thermodynamics. 57 (2013) 470-476. http://dx.doi.org/10.1016/j.jct.2012.09.024